Journal of Nuclear Medicine, published on October 13, 2022 as doi:10.2967/jnumed.122.264453

A Realistic Multi-region Mouse Kidney Dosimetry Model to Support the Preclinical Evaluation of Potential Nephrotoxicity of Radiopharmaceutical Therapy

Clarita Saldarriaga Vargas[1,2], Lara Struelens[1], Matthias D'Huyvetter[2], Vicky Caveliers[2], Peter Covens[2].

[1]Radiation Protection Dosimetry and Calibrations, Belgian Nuclear Research Centre (SCK CEN), Mol, Belgium.

[2]Department of Medical Imaging, Laboratory for In Vivo Cellular and Molecular Imaging, Vrije Universiteit Brussel, Brussels, Belgium.

First author and corresponding author:

Clarita Saldarriaga Vargas

Belgian Nuclear Research Centre (SCK CEN)

Boeretang 200, 2400 Mol, Belgium

T: +32 476783102

E: csvargas@sckcen.be

Word count: 5000

Running title: A Multi-region Model of a Mouse Kidney

ABSTRACT

Sub-organ absorbed dose estimates in mouse kidneys are crucial to support preclinical nephrotoxicity analyses of alpha- and beta-particle emitting radioligands exhibiting a heterogeneous activity distribution in kidney. This is however limited by the scarcity of reference dose factors (*S* values) available in the literature for specific mouse kidney tissues. **Methods:** A computational multi-region model of a mouse kidney was developed based on high-resolution magnetic resonance imaging data from a healthy mouse kidney. The model was used to calculate *S* values for 5 kidney tissues (cortex, outer and inner stripes of outer medulla, inner medulla, and papilla and pelvis) for a wide range of beta or alpha emitting radionuclides (45 in total) interesting for radiopharmaceutical therapy, using Monte Carlo calculations. Additionally, the application of regional *S* values was demonstrated for a ^{131}I-labelled single-domain antibody fragment with predominant retention in the renal outer stripe. **Results:** The heterogeneous activity distribution in kidneys of considered alpha and low to medium energy beta emitters considerably affected the absorbed dose estimation in specific sub-organ regions. The sub-organ tissue doses resulting from the non-uniform distribution of the ^{131}I-labelled antibody fragment largely deviate (from -40% to 57%) from the mean kidney dose resulting from an assumed uniform activity distribution throughout the whole kidney. The absorbed dose in the renal outer stripe was about 2.0 times higher than in the cortex and in the inner stripe, and about 2.6 times higher than in inner tissues. **Conclusion:** The use of kidney regional *S* values allows a more realistic estimation of the absorbed dose in different renal tissues from therapeutic radioligands with a heterogeneous uptake in kidneys. This constitutes an improvement from the simplistic (less accurate) renal dose estimates assuming a uniform distribution of activity throughout kidney tissues. Such improvement in dosimetry is expected to support preclinical studies essential for a better understanding of nephrotoxicity in humans. The dosimetric database represents an added value in the development of new molecular vectors for radiopharmaceutical therapy.

Keywords: multi-region mouse kidney model; sub-organ dosimetry; radiopharmaceutical therapy; MIRD; autoradiography.

INTRODUCTION

In radiopharmaceutical therapy the transit and temporary retention of radioligand in the kidneys during renal elimination results in a local irradiation of kidney tissues which can cause absorbed dose-limiting nephrotoxicity. Consequently, nephrotoxicity is often the focus of absorbed dose-escalation studies performed on mice during the preclinical testing of (novel) radioligands and the preclinical investigation of treatment optimization strategies beyond radioligand design. Additionally, the distribution of radioligand is often not uniform in the kidney (*1–3*). Small, fast-clearing radiopharmaceuticals often show an increased retention in the proximal tubules of the renal cortex and/or of the outer stripe of the outer medulla (cf. Figure 1) (*2,4,5*). This can lead to a corresponding non-uniform distribution of absorbed dose and tissue damage across renal regions (*1,6*) and even the specific substructures within them (*7*), particularly for radionuclides emitting charged-particle radiation with limited penetration range in tissue, like alpha particles, and low-to-medium-energy electrons and beta particles.

Accurate dosimetry of specific mouse kidney tissues is essential for interpreting the outcomes of preclinical nephrotoxicity studies. Understanding the impact in nephrotoxicity of the (local) tissue damage resulting from the non-uniform dose distribution of radiopharmaceuticals is of increased importance in kidney tissues, which have a complex functional architecture and potentially differ in radiobiological response (*8*). An aspect that precludes a more realistic kidney-tissue dosimetry of heterogeneous radioligand distributions is the scarcity of reference radionuclide *S* values (factors of absorbed dose per radionuclide decay) for relevant tissue regions of the mouse kidney. *S* values are dependent on the radionuclide radiation emissions and the geometry of the anatomical model used for modelling the radiation source and for absorbed dose calculations. Some dosimetry models of murine kidneys exist which allow to account to some extent for non-uniform distributions of radionuclides (*1,5,6*). Their application in preclinical studies is however limited by the few compartments used to represent the renal

structure and consequently the heterogeneity of the organ activity distribution. Furthermore, *S* values are available only for a limited number of radionuclides.

The aim of this work was to develop a computational realistic multi-region model of a mouse kidney, based on high-resolution magnetic resonance (MR) imaging data, to facilitate sub-organ kidney dosimetry in preclinical investigations of radiopharmaceutical therapy. Next, the model is used to calculate sub-organ regional *S* values of the kidney for a wide range of radionuclides of interest in radiopharmaceutical therapy. Finally, sub-organ kidney dosimetry is demonstrated for a single-domain antibody fragment (sdAb) radiolabeled with ^{131}I with predominant retention in the outer stripe of the renal outer medulla, and which is currently being evaluated clinically for radiopharmaceutical therapy of cancer expressing the human epidermal growth factor receptor type 2 (HER2) (*9*).

MATERIALS AND METHODS

A condensed description of the materials and methods is described below. The more detailed version can be found in the online supplemental data.

All animal experiments were conducted in accordance with the guidelines and after approval of the Ethical Committee of the Vrije Universiteit Brussel.

Development of Kidney Model

A schematic overview of the main steps involved in the development of the 3D kidney model is shown in Figure 2.

The kidney model was developed using as a reference high-resolution (43x78x78-µm voxels) MR imaging data obtained *ex vivo* on a perfusion-fixed kidney excised from a healthy mouse (C57BL/6, female, 9-weeks old, 19.5 g body weight). MR imaging was performed with a horizontal 7-T preclinical scanner (PharmaScan; Bruker BioSpin).

Ten volume regions were segmented on the MR image using the 3D-Slicer software (http://www.slicer.org). The segmented regions correspond to 4 tissues of the kidney parenchyma (the cortex, the outer stripe of the outer medulla (OSOM), the inner stripe of the outer medulla (ISOM) and the inner medulla (IM)), the major component of the vasculature within the kidney parenchyma, the papilla, the renal pelvis, part of the external renal vessels, part of the ureter and a uniform surrounding tissue. The kidney model was created by merging all the segmented regions into a single 3D matrix consisting of 127x62x125 (~ 1 million) voxels, with same voxel dimensions as the MR dataset.

Tissue segmentation was validated against regions of interest (ROI) drawn on conventional histology images of the same kidney.

Calculation of *S* Values and Energy Absorbed Fractions

$S(r_T \leftarrow r_S)$ values and energy absorbed fractions (φ) of different kidney tissues were calculated for the kidney model using Monte Carlo radiation transport simulations with MCNP6.2 (Los Alamos National Laboratory).

Monte Carlo calculations were performed for 12 beta-emitting radionuclides (^{32}P, ^{47}Sc, ^{67}Cu, ^{89}Sr, ^{90}Y, ^{131}I, ^{153}Sm, ^{161}Tb, ^{166}Ho, ^{177}Lu, ^{186}Re and ^{188}Re) and for the alpha emitters shown in Supplemental Figure S1 (decay schemes of ^{225}Ac, ^{227}Th, ^{230}U, ^{224}Ra, ^{211}At and ^{149}Tb) and their progeny, which includes alpha, beta- and/or positron emitters. Radionuclide radiation emission data of ICRP Report 107 (*10*) was used for modelling the radiation sources. Energy absorbed fractions for self-irradiation were calculated for monoenergetic electrons (20–2500 keV), alpha particles (3–10 MeV) and photons (10–1500 keV).

Source regions (r_S) and target regions (r_T) for *S*-value and absorbed-fraction calculations include: the renal cortex including its vasculature (*C*), the outer stripe of the outer medulla including its vasculature (*OS*), the inner stripe of the outer medulla (*IS*), the inner medulla including some vasculature (*IM*) and the renal papilla and pelvis (*PP*). These regions, all together, represent the whole kidney region (*K*), which was

used also as a source and target region in case of a uniform activity distribution throughout kidney tissues. For each radionuclide, the activity was uniformly distributed in each of the source regions and the absorbed dose per decay was simulated.

Kidney Dosimetry Study

A dosimetry study was performed to demonstrate the use of the *S* values calculated with the kidney model. The radioligand used to derive the mouse kidney biodistribution was the iodinated sdAb 2Rs15d (^{131}I-sdAb) (*11*).

Healthy mice (*n*=5, C57BL/6, female, 9-week-old, 20.7 ±1.0 g mean ± standard deviation (SD)) were anesthetized by inhalation with 2% isoflurane and were intravenously injected in the tail vein with 13.0 ± 3.3 MBq ^{131}I-sdAb (5 µg sdAb). At 1, 3, 6, 24 and 70 h post injection (p.i.), mice (*n*=1 per time point) were euthanized by cervical dislocation. The kidneys were dissected, weighed and their activity was measured in a gamma counter using an optimized measurement protocol (*12*). The fraction of injected activity per gram of dissected kidney tissue (*FIA/g*) was calculated.

The sub-organ distribution of ^{131}I-sdAb in kidney tissues was determined with high-resolution quantitative digital autoradiography using an iQID system (*13*). Each autoradiography image was quantified in ImageJ-Fiji (https://imagej.net/software/fiji/) using detailed ROIs drawn on histological images of the same section used for autoradiography or an adjacent kidney section. A ROI was drawn on each of the 5 tissues considered as source regions in the kidney model (r_S: *C*, *OS*, *IS*, *IM*, *PP*) and the mean of the counts per minute (CPM) of the ROI pixels were estimated.

Sub-organ regional dosimetry of kidney tissues was performed following the MIRD methodology. Two source distributions were considered: (i) a time-dependent non-uniform activity distribution based on the relative autoradiography data, and (ii) the simplified case in which activity is assumed to be uniformly distributed throughout kidney tissues (*i.e.,* r_S=r_T=*K*).

For each time point, the absorbed dose rate in each target region r_T delivered by the activities measured in each source regions r_S of the kidney model was calculated based on the *S* values calculated for the proposed kidney model. The activity of the whole kidney was determined with gamma counting and the relative sub-organ distribution of activity measured with autoradiography (for (i) only).

Absorbed dose rates as a function of time were analyzed by nonlinear least squares fitting (MATLAB, MathWorks) to a negative power function of time after injection. For each of the two source distributions considered, the absorbed dose per unit of administered activity ($D(r_T)/A_0$) was estimated for each target region applying mathematical integration of dose rate values from the time of injection (t=0) to infinity.

RESULTS

Kidney Model

There is a good agreement between the histology-based tissue ROIs and the MR-based ROIs used to define the kidney model (Figure 3 A, with additional comments in the supplemental data).

The main orthogonal dimensions of the kidney model are around 5.3x4.6x9.5 mm (excluding ureter and external vessels). In mouse kidneys, contrary to human kidneys, medullary tissues are not organized in multiple pyramids and form instead a single bean-shaped body (cf. Figure 3) (*14*). As such, there are no renal calyces, and a single renal papilla connects directly and deeply with the renal pelvis. The cortex and the OSOM appear as adjacent rims (each with a thickness of ~ 0.6 mm) surrounding most of the inner tissues. The masses and percentage volume occupancy of each tissue region are listed in Table 1. The 3D dataset of the kidney model can be found in the supplemental file Kidney_model_dataset.nii (available online).

S Values

S values for the considered alpha and beta emitting radionuclides are listed in Tables S1, S2 and S3 of the supplemental data. The simulation statistical error of all the reported *S* values was within 3%, unless otherwise specified. A subset of the *S* values is graphically shown in Figure 4 for a selection of beta and alpha emitters (and their progeny). The energy absorbed fractions for electrons, alpha particles and photons are shown in Supplemental Figure S2.

High-energy beta emitters (e.g., ^{90}Y, ^{188}R, ^{32}P) typically result in higher *S* values and more cross-irradiation between the source tissue and surrounding tissues than low-energy beta emitters (e.g., ^{177}Lu, ^{67}Cu, ^{161}Tb, ^{131}I). Cross-irradiation is nevertheless substantial also for low-energy beta emitters, particularly between adjacent target–source kidney tissue regions (e.g., *C*←*OS*, *IS*←*OS*). The *S* values for self-irradiation (e.g., *C*←*C*, *OS*←*OS*) are somewhat higher for radionuclides with an abundant yield of Auger and internal-conversion electrons (^{161}Tb, ^{153}Sm, ^{166}Ho), as these typically low-energy electrons are absorbed more locally than the more energetic beta particles (cf. Supplemental Figures S2 and S3).

The energy emitted by alpha emitters is absorbed mostly within the source region itself and cross-irradiation is small between adjacent tissues and negligible between more distant tissues (e.g., *IS*←*C*, *IM*←*OS*). Indeed, the absorbed fractions for self-irradiation with alpha particles are mostly ≥ 0.90 for most tissue regions (see Supplemental Figure S2).

Kidney Dosimetry Study

The pharmacokinetics of the ^{131}I-sdAb in mouse kidney tissues are fast. The kidney uptake after 24 h of ^{131}I-sdAb administration is less than 0.5% of the uptake at 1 h p.i. (Supplemental Table S4). The autoradiography images (Figure 5) clearly indicate a non-uniform and time-dependent biodistribution. During the first 24 h after radioligand administration, a prominent retention is observed in the OSOM tissue, followed by the cortical tissue (Supplemental Table S4). This is likely due to a partial reabsorption of the ^{131}I-sdAb in the proximal tubules located exclusively in these two tissues, and particularly in the

straight segments which densely occupy the OSOM (Figure 1). From 24 h p.i. onwards, the little activity that remains in the kidney is more concentrated in the cortex region, although the non-uniformity across tissues is less pronounced than at earlier time points. The concentration of activity in the inner tissues (ISOM, papilla and pelvis) is always lower than that in the cortex and OSOM.

The distribution of ^{131}I-sdAb activity in kidney tissues has a substantial impact on the estimation of the time-dependent absorbed dose rates (Figure 6 B) and the absorbed doses (Table 2), per unit of injected activity, in specific kidney tissues. Compared with the more realistic non-uniform source distribution, the assumption of a uniform distribution of activity throughout the kidney tissues (r_S=r_T=K) results in a strong underestimation of the absorbed dose rate in the OSOM and an overestimation of the absorbed dose rate in the other tissues (including the cortex) at early time points (< 24 h p.i.). A similar effect results in the absorbed doses, because for ^{131}I-sdAb the high activities at early time points dominate the estimation of the time-integrated absorbed dose. The absorbed dose in the OSOM is about 2.0 times higher than in the cortex and in the ISOM, and about 2.6 times higher than in inner tissues.

DISCUSSION

The calculated regional *S* values indicate that considering the heterogeneity of the activity distribution in mouse kidneys can have a considerable impact on the absorbed dose estimations of specific tissues, particularly for radionuclides that emit alpha particles and low to medium-energy beta particles. This was demonstrated for the non-uniform mouse kidney biodistribution of a ^{131}I-labelled sdAb which is predominantly and temporarily retained in the OSOM. ^{131}I emits low-to-medium-energy beta particles (182 keV, on average) with a short penetration range in tissue (~ 0.4 mm, on average) when compared with the size of mouse kidney tissues. Therefore, self-irradiation is the main contributor (~ 87%) to the absorbed dose rates to the OSOM at early time points (see Supplemental Figure S4). This holds true also

for the cortex (~ 71% from self-irradiation), although with an also important contribution (~ 29%) of cross-irradiation from activity located in the OSOM. This leads to a substantial non-uniform absorbed dose distribution across different kidney tissues in which the OSOM is the most irradiated tissue.

This study presented a realistic 3-dimensional model of mouse kidney tissues useful for preclinical internal radiation dosimetry. The regional *S* values calculated with the proposed model allow a more detailed and realistic estimation of absorbed doses in different renal tissues from beta- and alpha emitters, accounting for the heterogeneous activity distribution. To exploit the full potential of the proposed model requires information on the sub-organ activity distribution at the regional tissue level as a function of time. Such information can be derived from *ex vivo* mouse biodistribution studies using quantitative high-resolution autoradiography of beta and/or alpha particles of tissue sections of mice sacrificed at different sampling time points, complemented with gamma counting of the whole kidney to measure kidney activity, as demonstrated in this study. Alternatively, quantitative emission tomography imaging can be used to measure kidney activity thoroughly over time and *in vivo* (*12*), which would enable longitudinal studies (such as nephrotoxicity studies) on the same mice used for (organ-level) pharmacokinetic assessment. In such case, autoradiography measurements may be performed (on separate mice) at selected time points of the pharmacokinetic profile, chosen e.g. to sample regions of high activity and/or where the sub-kidney distribution is more likely to vary (absorption, distribution, elimination phases). The mouse kidney model may be seen as an analogue of the model of a human kidney presented in MIRD Pamphlet 19 (*3*), with some differences being that the former is used for preclinical dosimetry of mouse tissues and provides a more realistic representation of kidney tissues which additionally considers the OSOM as a separate source/target compartment. Modelling of OSOM tissues is pertinent for dosimetry in view of the possible substantial radioligand retention in the straight segments of the proximal tubules, which physically extend from the cortex to the OSOM in both humans and rodents. The early biodistribution of ^{131}I-sdAb considered here for the dosimetry study is a good example of such a situation.

For alpha-particle emitters, sub-regional dosimetry at the level of mouse nephron substructures (e.g., glomerulus and specific segments of the tubule) can be of interest. Although miniaturized versions of models of a human nephron can be used for that purpose (*7*), their use in preclinical investigation of radiopharmaceuticals is limited by the difficulty to determine the distribution of radionuclide activity at the level of nephron substructures. The intermediate (i.e., regional) dosimetry of alpha-particle emitters achievable with the regional *S* values presented here might be useful when sub-organ activity information is available only at a more regional (tissue) level.

S factors are sensitive to the target tissue mass and to the energy absorbed fraction, which is sensitive to the target–source geometry. Besides, the size of kidney tissues may vary with mouse strain, age, health condition, etc. Because of this, inaccuracies in absorbed dose estimations might arise from anatomical differences between the kidney model and the kidneys of mice used in preclinical studies. Mass scaling of the regional *S* values to the actual (measured) mass of the kidney (cf. factor $M_K/\bar{M}_{kidney}$ in Equation S1) can compensate for the effect of the target tissue mass in the absorbed dose estimations, assuming that the volumes of occupancy of the measured tissues is the same as in Table 1. However, mass scaling does not account for deviations in the absorbed fractions due to e.g. differences in the thickness of the cortical or the OSOM rims associated with tissues with distinct size or volume of occupancy than the kidney model. The impact of these factors may be investigated using simplified models (such as those based on ellipsoidal shells to represent tissue compartments (*6*)) and, if relevant, correction factors to be applied to absorbed dose estimations with the regional *S* values reported here may be determined. Such analyses were beyond the scope of this study.

Svensson *et al* used a stylized three-region 0.15-g-kidney model based on spheroids to calculate regional energy absorbed fractions for ^{177}Lu and ^{90}Y beta particles emitted by the cortex region (*5*). Compared with that model, the ^{177}Lu and ^{90}Y beta-particle absorbed fractions calculated with the more realistic model proposed in this study are respectively 6% and 19% lower for a self-irradiation of the cortex

256 (φ equal to 0.79 for ^{177}Lu and 0.23 for ^{90}Y), and 62% and 36% higher, for a cross-irradiation between the
257 cortex and the OSOM (φ equal to 0.082 for ^{177}Lu and 0.10 for ^{90}Y). These dosimetric discrepancies are likely
258 related to differences in geometry and size of kidney tissue regions between the two models.

259 More realistic absorbed dose estimates of mouse kidney tissues can support the analysis of preclinical
260 nephrotoxicity studies of therapeutic radioligands, such as the investigation of absorbed dose thresholds
261 for toxicity of specific kidney tissues (or substructures) resulting from non-uniform irradiations with
262 radionuclides (*5*,*6*,*8*). Such insight can be relevant for the design of first-in-human trials with novel
263 radioligands, by informing about potential toxicities due to the predicted absorbed dose distribution in
264 larger kidney tissues such as in human. The glomeruli are sometimes thought to be the absorbed dose-
265 limiting renal substructures when dealing with beta- radio-therapeutics (*8,15*). Yet, loss of proximal
266 tubules has (also) been associated with long-term nephrotoxicity in mice with either beta or alpha-emitting
267 radioligands (*5,16*). Investigating the absorbed dose dependence of glomerular and proximal tubular
268 damage is therefore of high interest and would benefit from more detailed dosimetry at the level of sub-
269 organ regions or even at the level of nephron substructures. Additionally, (back) translational research on
270 the renal absorbed dose–toxicity relationships might support the investigation of treatment optimization
271 strategies beyond radioligand design, such as renoprotective agents that reduce reabsorption and
272 internalization by the proximal tubule cells (*4,5*) and activity fractionation (*8,15*).

273 An improved understanding of radiation induced nephrotoxicity in the presence of absorbed dose (and
274 dose-rate) heterogeneity after radiopharmaceutical therapy should improve the implementation of
275 optimized and patient-specific procedures (*8*). In peptide receptor radionuclide therapy, for example, the
276 microscopic absorbed dose distribution in human kidneys is thought to play a role in the seemingly lower
277 incidence of nephrotoxicity of ^{177}Lu-labelled somatostatin analogues when compared with similar ^{90}Y-
278 labelled peptides (*2,17*). Clinical investigation of the influence of absorbed dose non-uniformity on
279 nephrotoxicity is however a challenge, as it would require the availability of a large amount of good-quality

patient-specific detailed dosimetry and response data of the kidneys for each therapeutic setting (*18*). Conversely, animal experiments allow to determine the microscopic distribution of radiopharmaceuticals in tissues *ex vivo* and to investigate the biological response associated with radiopharmaceutical therapy in a more reproducible and controlled experimental setting. The *S* values for regions of the mouse kidney presented here could facilitate preclinical absorbed dose estimations required to investigate the contribution to nephrotoxicity of the absorbed dose-dependent damage to different kidney tissues resulting from the (non-uniform) distribution of radiopharmaceuticals. Such kind of investigations will be essential in the development of complication probability biophysical models for nephrotoxicity in radiopharmaceutical therapy (*8*).

CONCLUSION

A computational multi-region model of a mouse kidney was developed and used to create a database of *S* values for 5 tissue regions and for a wide range of beta and alpha emitters of interest in radiopharmaceutical therapy. The comprehensive set of regional *S* values facilitates preclinical internal radiation dosimetry of mouse kidney tissues and allow a more realistic estimation of the doses absorbed by different renal tissues from therapeutic radioligands with a non-uniform distribution in kidneys, such as the ^{131}I-labelled single-domain antibody fragment investigated. The proposed model and the computed *S* values represent an improvement from the simplistic (less accurate) renal absorbed dose estimates assuming a uniform distribution of activity throughout the entire kidney. Such dosimetric improvement is expected to support preclinical nephrotoxicity studies essential for a better understanding (and prediction) of nephrotoxicity in humans.

DISCLOSURES

MD is employed by Precirix SA and holds ownership interest in sdAb therapeutics. MD is also a postdoctoral researcher of the Research Foundation Flanders - FWO (12H3619N). The other authors declare that they have no competing interests.

ACKNOWLEDGEMENTS

The authors kindly thank Cindy Peleman and Jos Eersels (VUB), Noami Daems, Jasmine Buset and Kevin Tabury (SCK CEN), and Brian Miller (University of Arizona), for technically assisting in the animal experiments, histology, microscopy or autoradiography; Jörn Engelmann and Elisabeth Jonckers (University of Antwerp) for the micro-MRI work.

KEY POINTS

QUESTION: How much does the non-uniform distribution of radionuclides used for radiopharmaceutical therapy impact the absorbed dose in mouse kidney tissues?

PERTINENT FINDINGS: A computational multi-region model of a mouse kidney was developed and was used to calculate *S* values for 5 kidney tissue regions for a wide range of beta- and alpha-particle emitters of interest in radiopharmaceutical therapy. The database of regional *S* values indicates that the consideration of an heterogeneous activity distribution in kidneys can have a considerable impact on the absorbed dose estimates in specific renal sub-structures, in particular when dealing with alpha and low-to-medium-energy beta particle emitters.

IMPLICATIONS FOR PATIENT CARE: An improved dosimetry of therapeutic radiopharmaceuticals in mouse kidney tissues will contribute to a better understanding and prediction of the nephrotoxicity in the presence of heterogeneous absorbed dose depositions in human kidneys.

REFERENCES

1. Flynn AA, Pedley RB, Green AJ, et al. The nonuniformity of antibody distribution in the kidney and its influence on dosimetry. *Radiat Res*. 2003;159:182-189.
2. Konijnenberg M, Melis M, Valkema R, Krenning E, de Jong M. Radiation dose distribution in human kidneys by octreotides in peptide receptor radionuclide therapy. *J Nucl Med*. 2007;48:134-142.
3. Bouchet LG, Bolch WE, Blanco HP, et al. MIRD pamphlet no. 19: absorbed fractions and radionuclide S values for six age-dependent multiregion models of the kidney. *J Nucl Med*. 2003;44:1113-1147.
4. Chigoho DM, Bridoux J, Hernot S. Reducing the renal retention of low- to moderate-molecular-weight radiopharmaceuticals. *Curr Opin Chem Biol*. 2021;63:219-228.
5. Svensson J, Mölne J, Forssell-Aronsson E, Konijnenberg M, Bernhardt P. Nephrotoxicity profiles and threshold dose values for [^{177}Lu]-DOTATATE in nude mice. *Nucl Med Biol*. 2012;39:756-762.
6. Konijnenberg MW, Bijster M, Krenning EP, de Jong M. A stylized computational model of the rat for organ dosimetry in support of preclinical evaluations of PRRT with ^{90}Y, ^{111}In, or ^{177}Lu. *J Nucl Med*. 2004;45:1260-1269.
7. Hobbs RF, Song H, Huso DL, Sundel MH, Sgouros G. A nephron-based model of the kidneys for macro-to-micro α-particle dosimetry. *Phys Med Biol*. 2012;57:4403-4424.
8. Wessels BW, Konijnenberg MW, Dale RG, et al. MIRD pamphlet No. 20 the effect of model assumptions on kidney dosimetry and response - implications for radionuclide therapy. *J Nucl Med*. 2008;49:1884-99.
9. D'Huyvetter M, De Vos J, Caveliers V, et al. Phase I trial of ^{131}I-GMIB-Anti-HER2-VHH1, a new promising candidate for HER2-targeted radionuclide therapy in breast cancer patients. *J Nucl Med*. 2021;62:1097-1105.
10. ICRP. Nuclear decay data for dosimetric calculations. ICRP publication 107. Ann. ICRP 38 (3). 2008.

11. D'Huyvetter M, De Vos J, Xavier C, et al. ^{131}I-labeled anti-HER2 camelid sdAb as a theranostic tool in cancer treatment. *Clin Cancer Res*. 2017;23:6616-6628.
12. Vargas CS, Struelens L, D'Huyvetter M, Caveliers V, Covens P. Assessment of mouse-specific pharmacokinetics in kidneys based on ^{131}I activity measurements using micro-SPECT. *EJNMMI Phys*. 2022;9:13.
13. Miller BW, Gregory SJ, Fuller ES, Barrett HH, Barber HB, Furenlid LR. The iQID camera: an ionizing-radiation quantum imaging detector. *Nucl Instrum Methods Phys Res A*. 2014;767:146-152.
14. Treuting PM, Kowalewska J. Urinary system. In: Treuting PM, Dintzis SM, eds. *Comparative Anatomy and Histology: A Mouse and Human Atlas*. Academic Press; 2012:229-251.
15. Barone R, Borson-Chazot F, Valkema R, et al. Patient-specific dosimetry in predicting renal toxicity with (90)Y-DOTATOC: relevance of kidney volume and dose rate in finding a dose-effect relationship. *J Nucl Med*. 2005;46 Suppl 1:99S-106S.
16. Kiess AP, Minn I, Vaidyanathan G, et al. (2S)-2-(3-(1-carboxy-5-(4-211At-astatobenzamido)pentyl)ureido)-pentanedioic acid for PSMA-targeted α-particle radiopharmaceutical therapy. *J Nucl Med*. 2016;57:1569-1575.
17. Bergsma H, Konijnenberg MW, van der Zwan WA, et al. Nephrotoxicity after PRRT with (177)Lu-DOTA-octreotate. *Eur J Nucl Med Mol Imaging*. 2016;43:1802-1811.
18. Strigari L, Konijnenberg M, Chiesa C, et al. The evidence base for the use of internal dosimetry in the clinical practice of molecular radiotherapy. *Eur J Nucl Med Mol Imaging*. 2014;41:1976-1988.

325

GRAPHICAL ABSTRACT

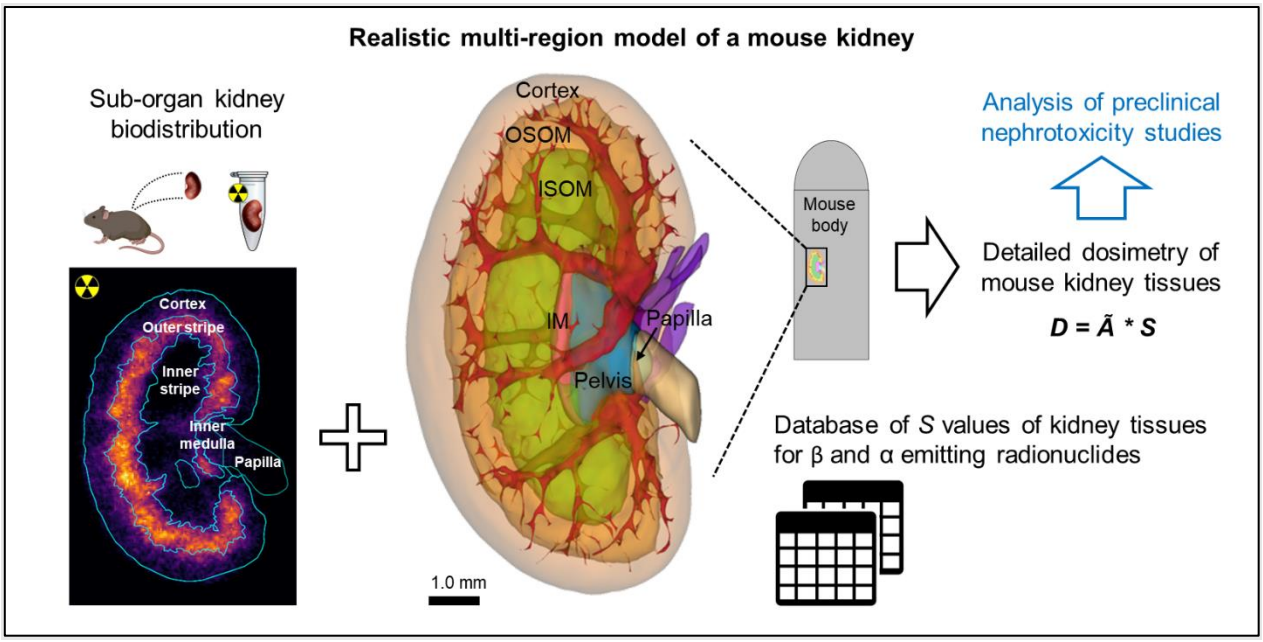

FIGURES

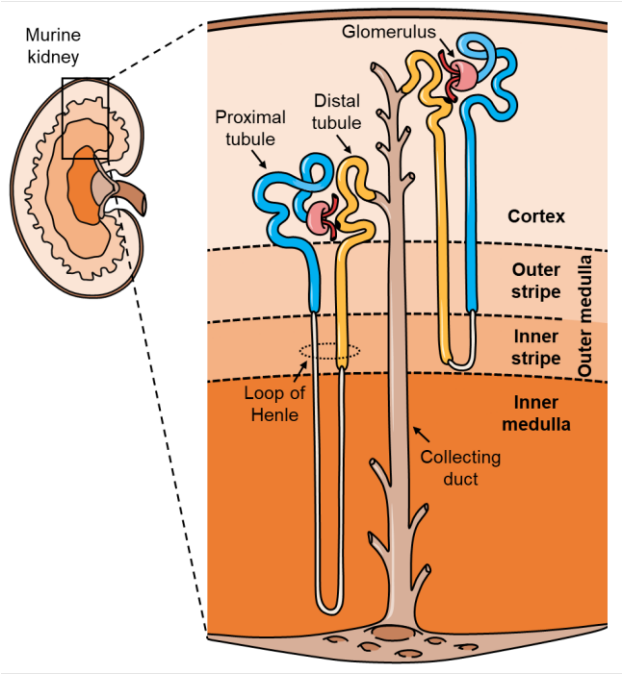

FIGURE 1. Microscopic anatomy of kidney tissues. The main nephron parts and the different kidney regions to which they belong are indicated.

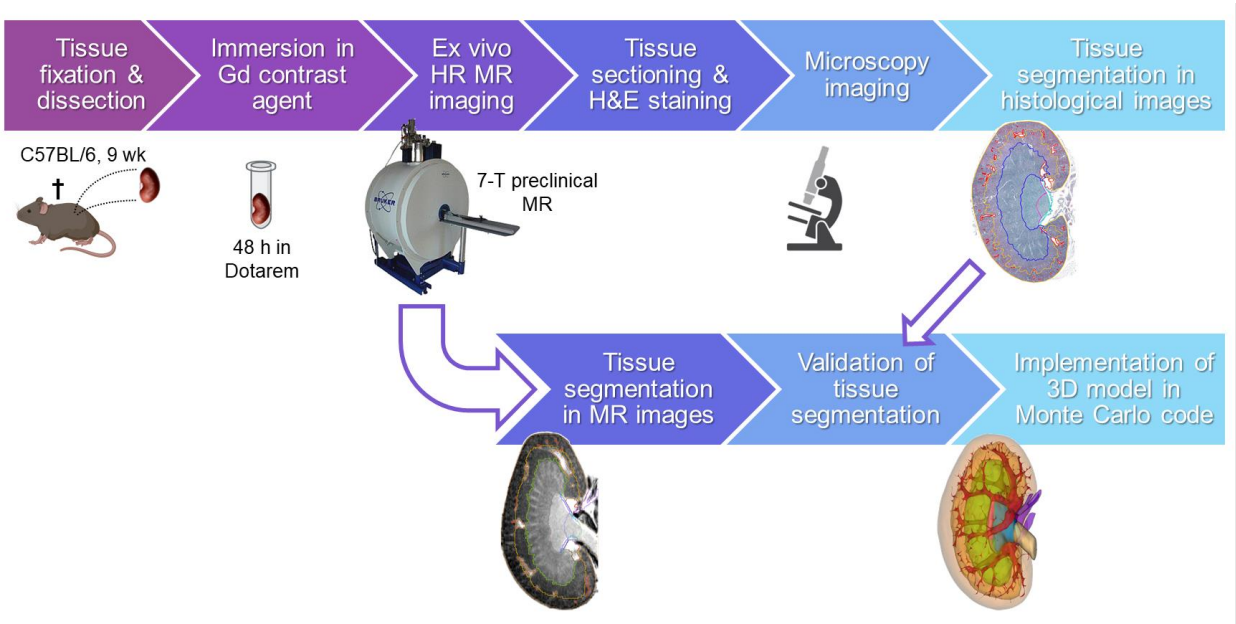

332

333 **FIGURE 2**. Workflow diagram of the development of the multi-region kidney model.

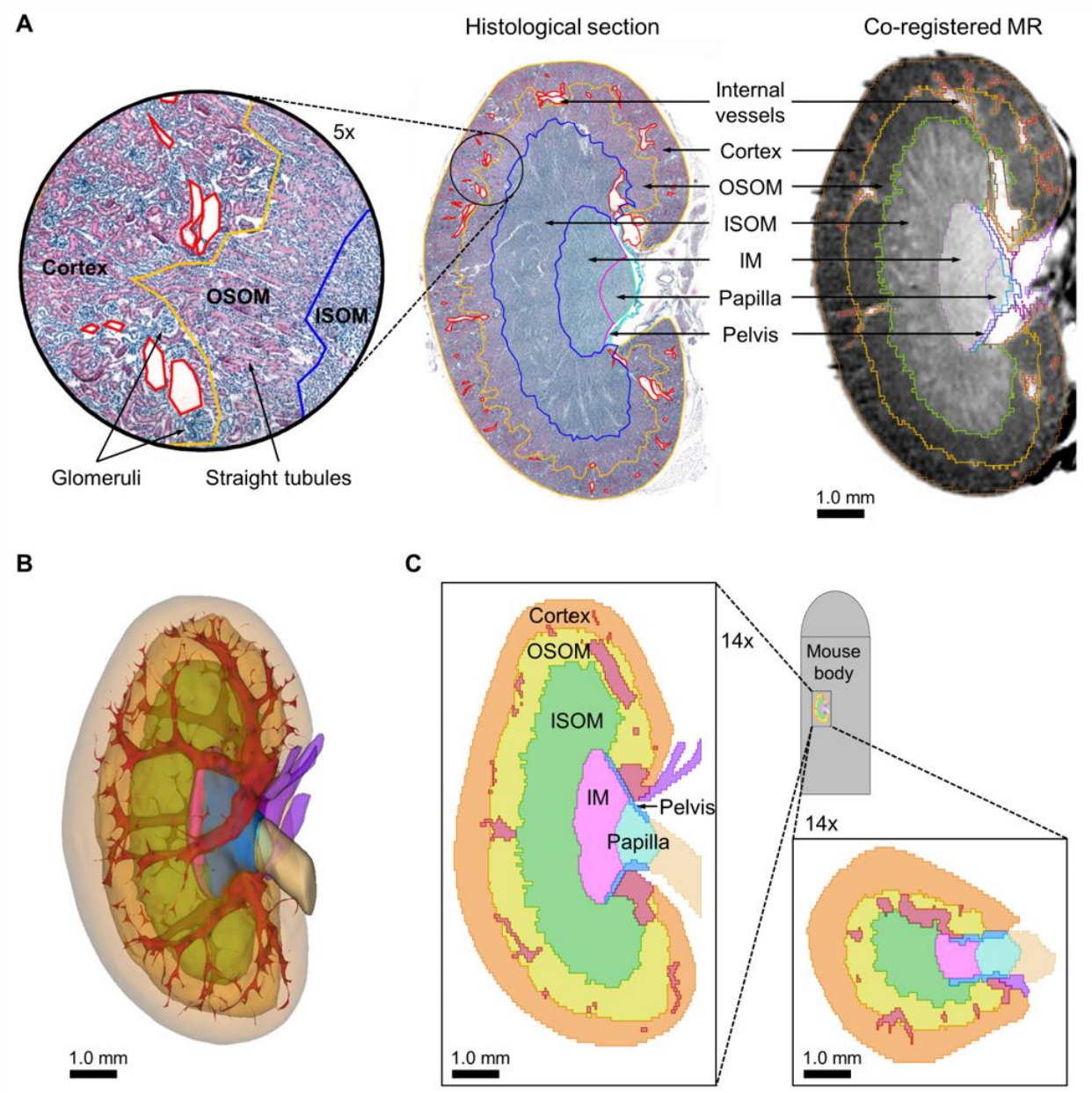

334

335 **FIGURE 3**. Validation of MR-based kidney-tissue segmentation against histology (**A**). Kidney model: 3D

336 rendering with transparency (**B**), and coronal (left) and transverse (bottom right) cross-section views of

337 the kidney lattice (**C**) as implemented in the Monte Carlo code.

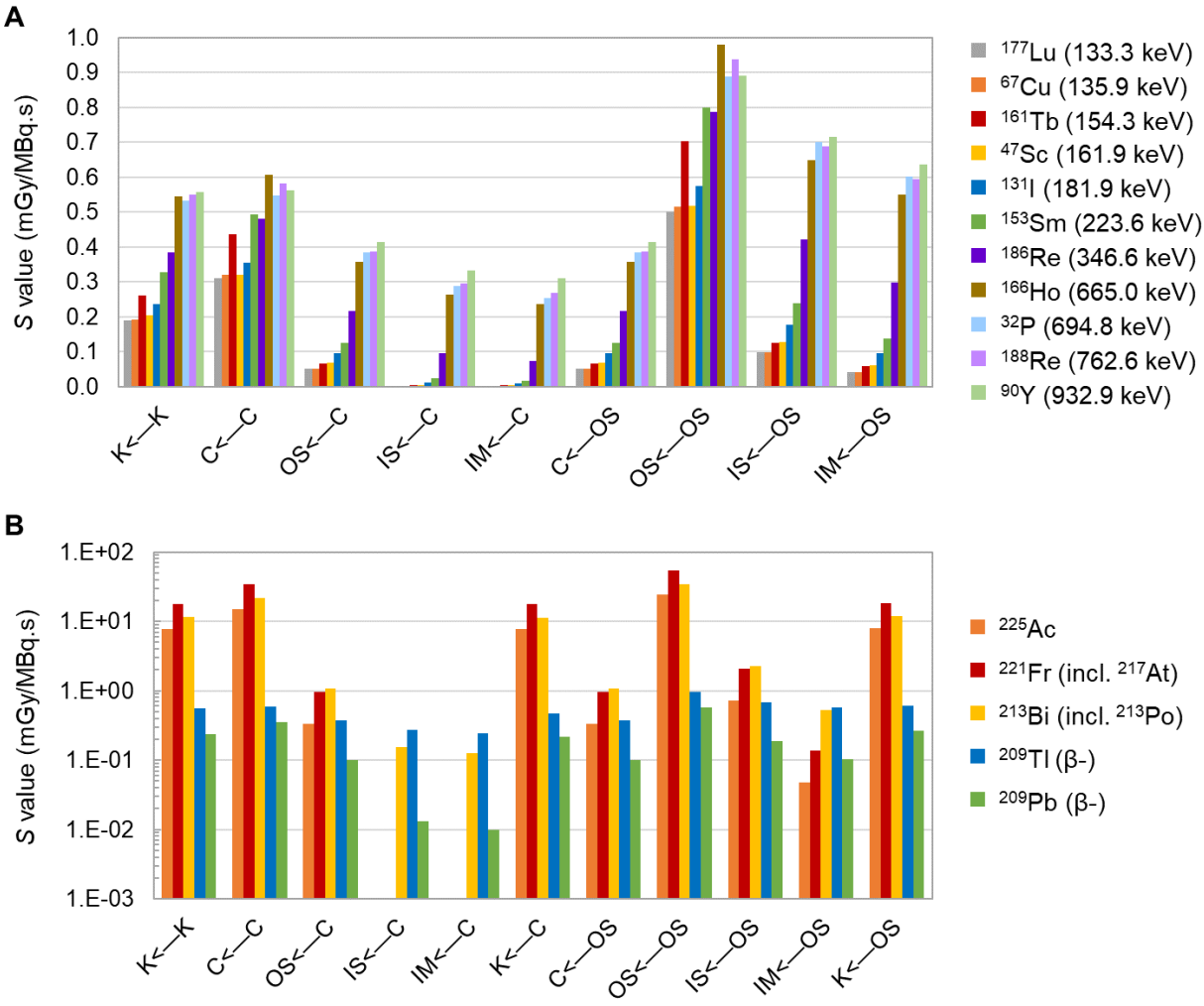

338

339 **FIGURE 4**. *S* values for some beta- emitters (**A**) and for ^{225}Ac and some of its progeny (**B**), for selected

340 source/target tissues. For convenience, the radionuclide series in sub-figure **A** are listed in order of

341 increasing mean beta-particle energy per beta decay (values in parenthesis in the series legends).

342

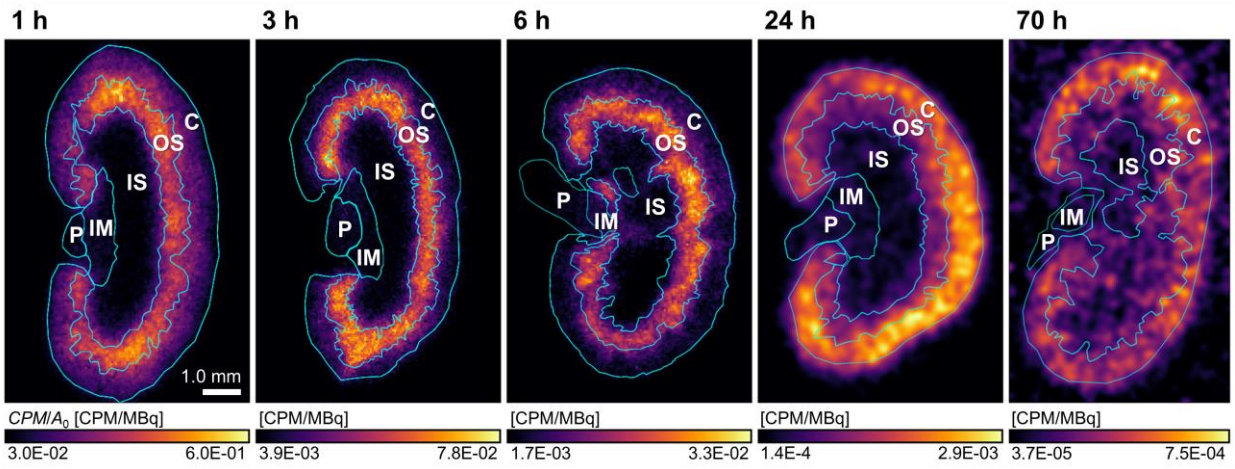

343

344 **FIGURE 5**. Autoradiography images of kidney tissues of mice sacrificed at 1, 3, 6, 24 and 70 h p.i. of ^{131}I-

345 sdAb. Autoradiography data at 24 and 70 h p.i. were smoothed with a 2.0-sigma Gaussian filter for

346 visualization only. ROIs used for quantification are shown in cyan color (C: cortex; IM: inner medulla; IS:

347 inner stripe; OS: outer stripe; P: papilla and pelvis).

348

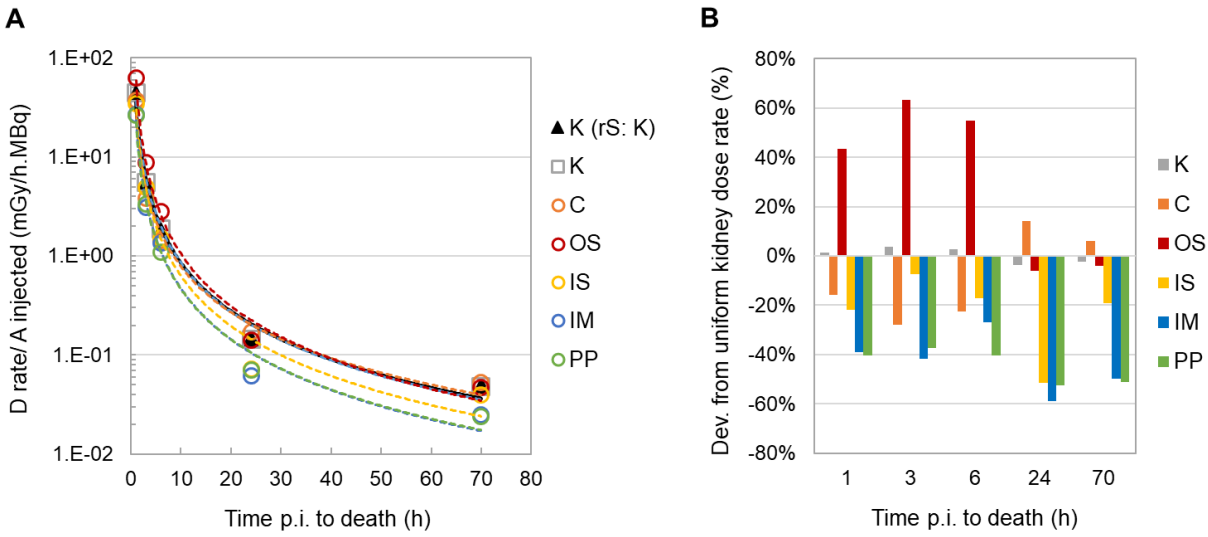

FIGURE 6. **A**: Dose rates per unit of injected activity in different tissue regions and in the whole kidney, as a function of time p.i. of ^{131}I-sdAb, for the heterogeneous activity distribution based on autoradiography data (Supplemental Table S4) and for an assumed uniform activity distribution throughout the kidney (r_S=*K*). The curves indicate the power function fit of each target region (cf. Supplemental Table S5). **B**: Percentage deviations from the uniform dose rate throughout kidney tissues (r_S=*K*).

TABLES

TABLE 1. Mass (*M*) and percentage volume occupancy (*%V*) of the kidney model regions used as source and/or target regions, including blood vessels.

r_T (or r_S)	*M* region (*mg*)	*M* vessels (*mg*)	*%V* region (*%*)
C	60.2	1.4	51%
OS	37.3	3.5	32%
IS	16.4	0.4	14%
IM	2.0	-	2%
PP	1.5	-	1%
K	117.5	5.3	100%

360 **TABLE 2**. Absorbed doses delivered to different tissue regions and to the whole kidney, per unit of
361 injected activity, for the heterogeneous activity distribution based on autoradiography data (Supplemental
362 Table S4) and for an assumed uniform activity distribution throughout the whole kidney.

	Heterogeneous A distribution						Uniform A (r_S=K)
	K	C	OS	IS	IM	PP	K
Absorbed dose per injected activity, $D(r_T)/A_0$ (mGy.MBq^{-1})	73.1	54.8	111.6	62.3	43.0	43.6	71.2
% dev. from $D(r_T=r_S=K)/A_0$ (%)	3%	-23%	57%	-12%	-40%	-39%	-

363

364

SUPPLEMENTAL DATA

Supplementary Methods – Development of the Kidney Model

For tissue fixation and dissection, the mouse was anesthetized with an overdose of ketamine-xylazine. Transcardial perfusion was performed with 0.1 M phosphate-buffered saline solution until the liver became brown and the fluid exiting the heart became clear, followed by a 4% PFA solution. Immediately after perfusion, the left kidney was excised from the mouse and was immersed in a 4% paraformaldehyde solution at 4 °C for one night for tissue preservation. Afterwards, the kidney was immersed for 48 hours in a 2.5 mM solution of Dotarem (gadolinium-based contrast agent; Guerbet) to enhance visibility of different renal tissues in the MR image. Lastly, the kidney was transferred to a phosphate-buffered saline with 0.1% of sodium azide for conservation and MR imaging.

MR imaging was performed at the Bio-Imaging Laboratory of the University of Antwerp (Belgium) with a horizontal 7-T preclinical scanner (PharmaScan; Bruker BioSpin) equipped with a homemade transmit receive linear volume resonator at 300 MHz using a T1-weighted rapid acquisition with relaxation enhancement (RARE) sequence (30-ms repetition time, 11-ms echo time, 100 excitations). The MR image resolution was 43x78x78 µm (anisotropic parallelepiped voxels).

Ten volume regions were segmented on the MR image using 3D Slicer software (http://www.slicer.org) both manually and with the aid of semi-automatic tools based on voxel intensity (e.g., threshold tool) and location (e.g., grow from seed tool) information. The segmented regions correspond to 4 tissues of the kidney parenchyma (namely the cortex, the outer stripe of the outer medulla (OSOM), the inner stripe of the outer medulla (ISOM) and the inner medulla (IM)), the major component of the vasculature within the kidney parenchyma, the papilla, the renal pelvis, part of the external renal vessels, part of the ureter and a uniform surrounding tissue. All segmented regions were merged into a single 3D matrix consisting of 127x62x125 (~ 1 million) voxels, with same voxel dimensions as the MR dataset.

Tissue segmentation was validated with conventional histology of the same kidney. To that end, after MR imaging, the kidney specimen was embedded in paraffin and sectioned (7-µm thickness) in the coronal plane. Sections were stained with hematoxylin and eosin (H&E) and were digitally imaged at 20x magnification using bright-field contrast on a Ti Eclipse inverted widefield microscope (Nikon Instruments Inc). Regions of interest (ROI) were drawn on the histological images over different kidney tissues and were visually compared against manually co-registered cross sections of the segmented 3D kidney model.

Supplementary Methods – Calculation of *S* Values and Energy Absorbed Fractions

The 3D segmentation matrix was implemented in MCNP as a lattice of parallelepiped elements (voxels) using same lattice and voxel dimensions as the segmentation map. That lattice containing the kidney model was embedded inside a 24-mL region representing the mouse body, modelled as an elliptical cylinder capped by a half ellipsoid. All mouse regions (body and lattice with kidney) were modelled as 1.04-$g.cm^{-3}$ soft tissue with elemental composition as in the adult human kidney model of MIRD Pamphlet 19 (*3*).

Radionuclide radiation emission data of ICRP Report 107 (*10*) was used for modelling the radiation sources. The simulated sources included photons (gamma- and X-rays), beta particles (beta- and positrons), Auger and internal conversion electrons and alpha particles. The kinetic energy of beta- particles and positrons emitted by the sources was sampled from a continuous spectrum based on linear interpolations of the energy–emission probability data of ICRP107.

MCNP cross-section libraries EPRDATA14 and EL03 for photon and single-event electron/positron transport were used. Alpha-particle transport was based on the continuous slowing down approximation for energy loss. The cut-off energy (i.e., the limit at which the particle energy is regarded to be locally absorbed) was set to 1 keV for all particles.

Source regions (r_S) and target regions (r_T) for *S* value and absorbed fraction calculations include: the renal cortex including its vasculature (*C*), the outer stripe of the outer medulla including its vasculature (*OS*), the inner stripe of the outer medulla (*IS*), the inner medulla including some vasculature (*IM*) and the renal papilla and pelvis (*PP*). These regions, all together, represent the whole kidney region (*K*), which was used also as a source and target region in case of a uniform activity distribution throughout kidney tissues.

For each radionuclide, the activity was uniformly distributed in each of the source regions and the absorbed dose per decay was simulated using MCNP *F8 tally. For the radionuclide chains involving alpha emitters, only the descendants with a half-life shorter than 1 year were considered descendants (radionuclides shown in black color in Supplemental Figure S1). Therefore, *S* values were not calculated for ^{207}Bi (descendant of ^{211}At) and for ^{210}Pb (descendent of ^{230}U) and its descendants. Also, the *S*-value contributions of short-lived (< 1 min) descendants of alpha emitters are included in the *S* values of the nearest parent isotope with a half-life longer than 1 min (radionuclides enclosed by a dashed line box in Supplemental Figure S1).

Monte Carlo simulations were performed in a parallel computer system (based on Intel Xeon Gold 6154 3.00 GHz processors running CentOS 7.8) using 72 threads. The number of source particles simulated for each radionuclide source region was at least 3.0E+06 for beta particles, 1.0E+07 for Auger and internal conversion electrons, 3.0E+07 for photons, and 1.0E+07 for alpha particles. As a reference, the computing times for 1.0E+06 simulated beta particles of ^{131}I and ^{90}Y emitted from the cortex region were respectively 15 and 70 minutes.

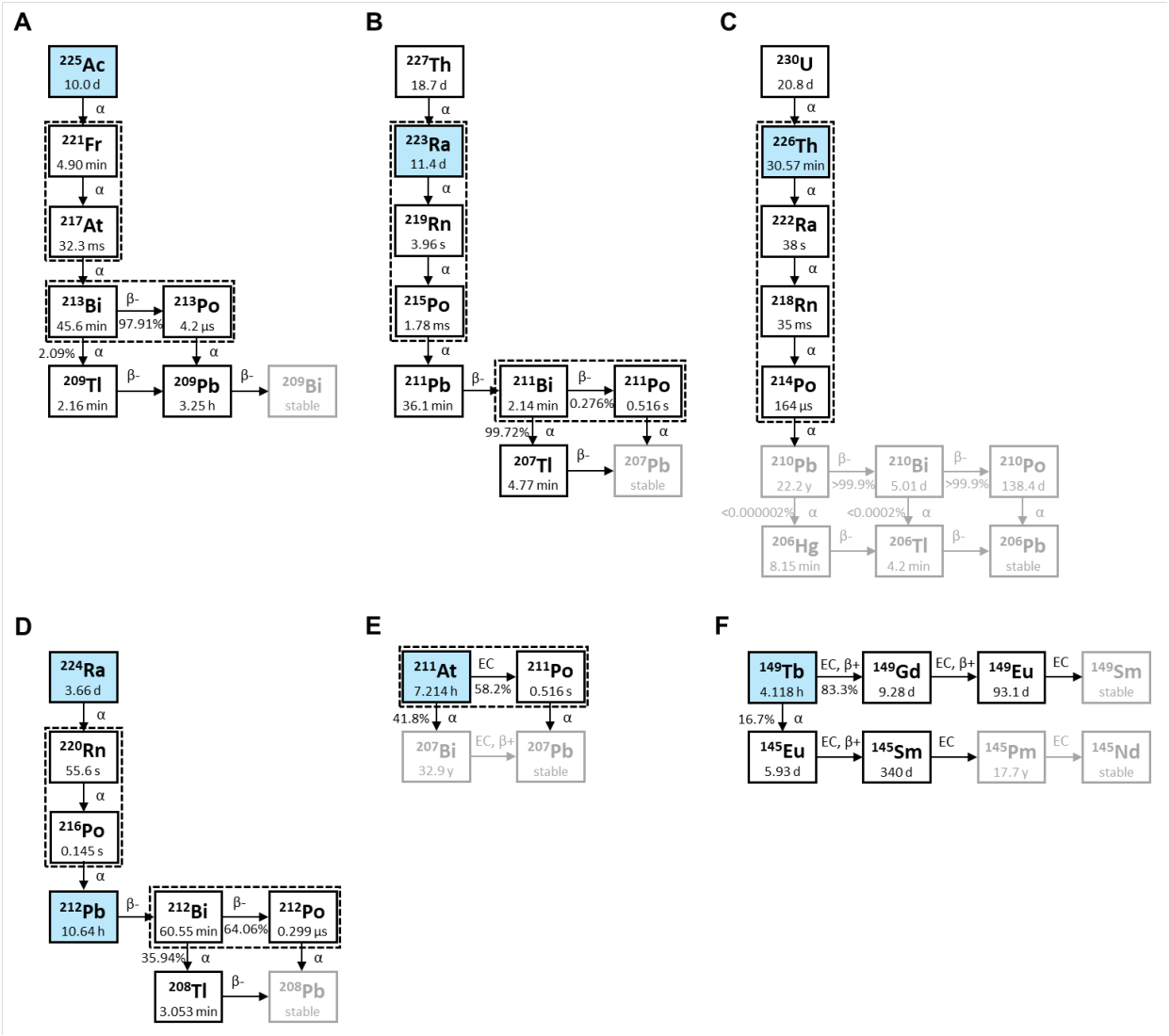

FIGURE S1. Decay schemes of various alpha emitters of interest in radiopharmaceutical therapy. The radionuclide decays enclosed by a dashed line box are considered as a single *S* value because of the short half-life (< 1 min) of the descendants.

Supplementary Methods – Kidney Dosimetry Study

A dosimetry study was performed to demonstrate the use of the regional *S* values calculated with the kidney model. The radioligand used to derive the mouse kidney biodistribution was the iodinated anti-HER2 sdAb 2Rs15d, previously reported elsewhere (*11*).

All reagents were purchased from Sigma-Aldrich unless otherwise stated. Sodium [^{131}I]iodide was purchased from Perkin-Elmer. Anti-HER2 sdAb 2Rs15d was radiolabeled with ^{131}I via the residualizing prosthetic group N-Succinimidyl 4-guanodinomethyl-3-[^{131}I]iodobenzoate ([^{131}I]SGMIB) and purified as reported previously (*11*).

Healthy mice (*n*=5, C57BL/6, female, 9-week-old, 20.7 ±1.0 g body-weight mean ± standard deviation (SD)) were anesthetized by inhalation with 2% isoflurane and were intravenously injected in the tail vein with 13.0 ± 3.3 MBq ^{131}I-sdAb (5 µg sdAb). At 1, 3, 6, 24 and 70 h post injection (p.i.), mice (*n*=1 per time point) were euthanized by cervical dislocation. The kidneys were dissected, weighed and their activity was measured in a Cobra-II 5003 gamma counter (Canberra-Packard) using an optimized measurement protocol (*12*). Radioactivity in kidney was corrected for decay to the time of sacrifice. The fraction of injected activity per gram of dissected kidney tissue (*FIA/g*) was calculated.

The sub-organ distribution of ^{131}I-sdAb in kidney tissues was determined with high-resolution quantitative digital autoradiography using an iQID system (*13*). To that end, the kidney specimens were snap-frozen and cryostat-sectioned in 10-µm sections. For the autoradiography measurements, tissue sections were placed in contact with a scintillating screen based on terbium-doped gadolinium oxysulfide (Gd_2O_2S:Tb) phosphor (Kodak BioMax TranScreen LE; Carestream Health), which was used to convert the beta and electron emissions of ^{131}I into visible photons detectable by the iQID camera. Tissue sections were imaged for up to 10 hours. The resulting autoradiography images were corrected for decay to the time of sacrifice using ImageJ-Fiji software (https://imagej.net/software/fiji/). Each autoradiography image was quantified in ImageJ-Fiji using detailed ROIs drawn on histological images (H&E staining) of the same section used for autoradiography or an adjacent kidney section. A ROI was drawn on each of the 5 tissues considered as source regions in the kidney model (r_S: *C*, *OS*, *IS*, *IM*, *PP*) and the mean of the counts per minute (CPM) of the ROI pixels were estimated (*CPM*(r_S)).

Sub-organ regional dosimetry of kidney tissues was performed following the MIRD methodology. Two source distributions were considered: (i) a time-dependent heterogeneous activity distribution based on the relative autoradiography data, and (ii) the simplified case in which activity is assumed to be uniformly distributed throughout kidney tissues (*i.e.,* r_S=r_T=*K*). For each time point, the absorbed dose rate ($\dot{D}(r_T, t)$) in each target region r_T delivered by the activities in each source regions r_S of the kidney model was calculated, per unit of administered activity (A_0), as:

$$\dot{D}(r_T, t)/A_0 = \frac{1}{A_0} \cdot \frac{M_K}{\bar{M}_{kidney}} \cdot \sum_{r_S} A(r_S, t) \cdot S(r_T \leftarrow r_S) \qquad \text{(Eq. S1)}$$

Where $A(r_S,t)$ is the activity in source region r_S at a time *t* p.i. of the radioligand; $S(r_T \leftarrow r_S)$ is the radionuclide-specific *S* value calculated for the proposed kidney model for the target/source regions r_T and r_S; M_K is the mass of region *K* of the kidney model (0.1175 g, cf. Table 1); and $\bar{M}_{kidney}$ is the average of the measured kidney masses of all (*n*=5) mice (0.1270 g). The kidney activities measured with gamma counting ($A(t)_{\text{kidney}}$) are affected by inter-mouse variability. To limit the effect of this in the dosimetry, normalized whole-kidney activities ($A(t)_{\text{kidney\_norm}}$) were calculated by multiplying the whole-kidney activities measured with

gamma counting ($A(t)_{kidney}$) by a normalization factor $M(t)_{kidney}/\overline{M}_{kidney}$ (where $M(t)_{kidney}$ corresponds to the measured kidney mass corresponding to time point t). When the activity is uniformly distributed throughout kidney tissues (r_S=K), $A(r_S,t)$ is equal to the normalized whole-kidney activity $A(t)_{kidney\_norm}$. To estimate $A(r_S,t)$ for the sub-kidney regions (Equation S2), the normalized kidney activity $A(t)_{kidney\_norm}$ was allocated to the different source regions of the kidney model according to the relative $CPM(r_S)$ values determined with autoradiography and the percentage volume occupancy of region r_S in region K of the kidney model ($\%V(r_S)$) (cf. Table 1).

$$A(r_S,t) = \%V(r_S) \cdot A(t)_{kidney\_norm} \cdot \frac{CPM_{r_S}}{\sum_{rS} CPM(rS)\cdot \%V(rS)} \qquad \text{(Eq. S2)}$$

Thus, the relative activity concentrations of the different compartments of the kidney model are assumed to be the same as the relative intensity densities of the different tissue ROIs of the autoradiography images.

Values of $\dot{D}(r_T,t)/A_0$ as a function of time elapsed p.i. (t) were analyzed by nonlinear least squares fitting (MATLAB, MathWorks). The Pearson's correlation coefficient (R^2) was used to quantify goodness of fit. Initially, various mathematical functions were considered for analyzing the time dependence of $\dot{D}(r_T,t)/A_0$, including negative exponentials with or without a positive baseline (mathematical form: $f(t) = a\cdot e^{(-b\cdot t)}$; $f(t) = a\cdot e^{(-b\cdot t)} + d$), a sum of two negative exponentials ($f(t) = a\cdot e^{(-b\cdot t)} + g\cdot e^{(-h\cdot t)}$), and a single negative power function with and without a positive baseline ($f(t) = c_1\cdot t^{-c2}$; $f(t) = c_3\cdot t^{-c4} + c_5$). A previous investigation (not reported in this work) evaluated the sensitivity of each function model to a few subsets of data points selected from a larger dataset of $\dot{D}(K,t)/A_0$ of the kidney for an assumed uniform activity in kidney tissues (e.g., data subsets considering variations in the number of time points or in the number of mice per time point). In that investigation, from the functions considered, the negative power function resulted in the lowest variability in the estimation of the time-integrated absorbed dose per unit of injected activity from the different subsets of dose rate data, and showed an R^2 very similar to that of other (more complex) function models (e.g. difference in R^2 of less than 0.004 compared to a bi-exponential model, for the subsets of data considered). The R^2 of the $\dot{D}(r_T,t)/A_0$ data of specific kidney tissues for the heterogeneous activity distribution showed similar results (difference in R^2 of less than 0.001 between bi-exponential and power fits). Therefore, in this study a negative power function of time t with two coefficients (c_1 and c_2) (Equation S3) was chosen to model the time dependence of all the $\dot{D}(r_T,t)/A_0$ datasets.

$$\dot{D}(r_T,t)/A_0 \cong c_1\, t^{-c_2} \qquad \text{(Eq. S3)}$$

For each of the two source distributions considered, the mean absorbed dose ($D(r_T)$) per unit of administered activity ($D(r_T)/A_0$) was estimated for each target region applying mathematical integration of dose rate values from the time of injection (t=0) to infinity in two parts. Absorbed dose rates were assumed to be zero at t=0 and to increase linearly over time until a peak value at t=1 h (earliest time point measured), which was calculated from the power function fit. From t=1 h until infinity, kidney uptake was assumed to follow the power function fit. (The dose contribution of the period of time from the last measured time point (70 h) until infinity was verified to be lower than the dose contribution resulting from assuming only physical ^{131}I decay from 70 h p.i. on).

Supplementary Results – Segmentation of the Kidney Model Regions

There is a good agreement between the histology-based tissue ROIs and the MR-based ROIs used to define the kidney model (Figure 3 A). The sharp contrast in the MR data of the IM and ISOM, the ISOM and OSOM, and the largest blood vessels and kidney parenchyma facilitated the delineation of the boundary between these tissues. However, because of the poor contrast in the MR data of cortical and OSOM tissues, the cortex–OSOM boundary in the kidney model is smoother than the microscopically detailed boundary defined in histological images based on the presence of glomeruli (zoom-in subfigure in Figure 3 A). Yet the dimensions and overall extension of the OSOM tissue are well represented in the kidney model. The level of detail with which the internal vasculature could be segmented is limited by the spatial resolution of MR data. Because of this, only part of the vasculature tree is represented in the kidney model, where the thickest vessels (cf. Figure 3 B) correspond to pairs of arteries and veins located close to each other.

TABLE S1. *S* values of beta- emitters.

$r_T \leftarrow r_S$	*S* values ($mGy.MBq^{-1}.s^{-1}$)											
	^{177}Lu	^{67}Cu	^{161}Tb	^{47}Sc	^{131}I	^{153}Sm	^{186}Re	^{89}Sr	^{166}Ho	^{32}P	^{188}Re	^{90}Y
K ← *K*	1.89E-01	1.93E-01	2.61E-01	2.03E-01	2.38E-01	3.28E-01	3.84E-01	4.85E-01	5.45E-01	5.34E-01	5.51E-01	5.56E-01
C ← *C*	3.10E-01	3.20E-01	4.36E-01	3.20E-01	3.56E-01	4.94E-01	4.81E-01	5.15E-01	6.06E-01	5.47E-01	5.83E-01	5.62E-01
OS ← *C*	5.28E-02	5.24E-02	6.68E-02	6.94E-02	9.53E-02	1.26E-01	2.17E-01	3.36E-01	3.58E-01	3.84E-01	3.87E-01	4.14E-01
IS ← *C*	2.38E-03	2.83E-03	4.26E-03	5.07E-03	1.23E-02	2.35E-02	9.53E-02	2.37E-01	2.63E-01	2.87E-01	2.95E-01	3.32E-01
IM ← *C*	2.25E-03	2.66E-03	3.78E-03	4.34E-03	9.94E-03	1.74E-02	7.28E-02	2.06E-01	2.36E-01	2.55E-01	2.69E-01	3.10E-01
PP ←*C*	1.94E-02	1.95E-02	2.52E-02	2.65E-02	3.91E-02	5.40E-02	1.14E-01	2.24E-01	2.53E-01	2.70E-01	2.83E-01	3.19E-01
K ← *C*	1.76E-01	1.81E-01	2.46E-01	1.87E-01	2.15E-01	2.97E-01	3.31E-01	4.10E-01	4.69E-01	4.50E-01	4.71E-01	4.76E-01
C ← *OS*	5.28E-02	5.24E-02	6.68E-02	6.94E-02	9.53E-02	1.26E-01	2.17E-01	3.36E-01	3.58E-01	3.84E-01	3.87E-01	4.14E-01
OS ← *OS*	5.00E-01	5.15E-01	7.04E-01	5.17E-01	5.75E-01	7.99E-01	7.86E-01	8.41E-01	9.80E-01	8.89E-01	9.37E-01	8.91E-01
IS ← *OS*	9.86E-02	9.80E-02	1.24E-01	1.29E-01	1.78E-01	2.40E-01	4.22E-01	6.23E-01	6.49E-01	7.00E-01	6.88E-01	7.15E-01
IM ← *OS*	4.27E-02	4.15E-02	5.78E-02	6.16E-02	9.59E-02	1.37E-01	2.99E-01	5.20E-01	5.51E-01	6.03E-01	5.95E-01	6.35E-01
PP ← *OS*	7.48E-02	7.54E-02	9.29E-02	9.56E-02	1.27E-01	1.66E-01	2.89E-01	4.64E-01	4.96E-01	5.32E-01	5.36E-01	5.69E-01
K ← *OS*	2.02E-01	2.06E-01	2.78E-01	2.20E-01	2.60E-01	3.56E-01	4.29E-01	5.41E-01	6.02E-01	5.94E-01	6.09E-01	6.14E-01
C ← *IS*	2.38E-03	2.83E-03	4.26E-03	5.07E-03	1.23E-02	2.35E-02	9.53E-02	2.37E-01	2.63E-01	2.87E-01	2.95E-01	3.32E-01
OS ← *IS*	9.86E-02	9.80E-02	1.24E-01	1.29E-01	1.78E-01	2.40E-01	4.22E-01	6.23E-01	6.49E-01	7.00E-01	6.88E-01	7.15E-01
IS ← *IS*	1.19E+00	1.22E+00	1.67E+00	1.25E+00	1.40E+00	1.94E+00	1.92E+00	1.93E+00	2.21E+00	2.00E+00	2.09E+00	1.93E+00
IM ← *IS*	1.91E-01	1.89E-01	2.42E-01	2.52E-01	3.47E-01	4.63E-01	7.87E-01	1.09E+00	1.12E+00	1.21E+00	1.17E+00	1.20E+00
PP ← *IS*	4.72E-02	4.82E-02	5.96E-02	6.18E-02	8.76E-02	1.26E-01	2.86E-01	5.32E-01	5.67E-01	6.19E-01	6.16E-01	6.58E-01
K ← *IS*	2.03E-01	2.07E-01	2.80E-01	2.23E-01	2.66E-01	3.68E-01	4.68E-01	6.15E-01	6.77E-01	6.79E-01	6.90E-01	6.97E-01
C ← *IM*	2.25E-03	2.66E-03	3.78E-03	4.34E-03	9.94E-03	1.74E-02	7.28E-02	2.06E-01	2.36E-01	2.55E-01	2.69E-01	3.10E-01
OS ← *IM*	4.27E-02	4.15E-02	5.78E-02	6.16E-02	9.59E-02	1.37E-01	2.99E-01	5.20E-01	5.51E-01	6.03E-01	5.95E-01	6.35E-01
IS ← *IM*	1.91E-01	1.89E-01	2.42E-01	2.52E-01	3.47E-01	4.63E-01	7.87E-01	1.09E+00	1.12E+00	1.21E+00	1.17E+00	1.20E+00
IM ← *IM*	8.37E+00	8.64E+00	1.19E+01	8.41E+00	9.05E+00	1.27E+01	1.07E+01	9.16E+00	1.13E+01	9.11E+00	9.95E+00	8.58E+00
PP ← *IM*	1.41E+00	1.43E+00	1.68E+00	1.70E+00	2.05E+00	2.52E+00	3.25E+00	3.53E+00	3.60E+00	3.71E+00	3.66E+00	3.51E+00
K ← *IM*	2.03E-01	2.07E-01	2.80E-01	2.23E-01	2.66E-01	3.67E-01	4.67E-01	6.26E-01	6.92E-01	6.95E-01	7.08E-01	7.20E-01
C ← *PP*	1.94E-02	1.95E-02	2.52E-02	2.65E-02	3.91E-02	5.40E-02	1.14E-01	2.24E-01	2.53E-01	2.70E-01	2.83E-01	3.19E-01
OS ← *PP*	7.48E-02	7.54E-02	9.29E-02	9.56E-02	1.27E-01	1.66E-01	2.89E-01	4.64E-01	4.96E-01	5.32E-01	5.36E-01	5.69E-01
IS ← *PP*	4.72E-02	4.82E-02	5.96E-02	6.18E-02	8.76E-02	1.26E-01	2.86E-01	5.32E-01	5.67E-01	6.19E-01	6.16E-01	6.58E-01
IM ← *PP*	1.41E+00	1.43E+00	1.68E+00	1.70E+00	2.05E+00	2.52E+00	3.25E+00	3.53E+00	3.60E+00	3.71E+00	3.66E+00	3.51E+00
PP ← *PP*	9.80E+00	1.01E+01	1.44E+01	9.65E+00	1.04E+01	1.50E+01	1.21E+01	1.03E+01	1.30E+01	1.02E+01	1.12E+01	9.56E+00
K ← *PP*	1.89E-01	1.93E-01	2.62E-01	2.04E-01	2.40E-01	3.32E-01	4.00E-01	5.29E-01	5.94E-01	5.87E-01	6.06E-01	6.18E-01

TABLE S2. *S* values of some alpha emitters and their decay progenies.

$r_T \leftarrow r_S$	*S* values ($mGy.MBq^{-1}.s^{-1}$)										
	^{225}Ac	^{221}Fr (incl. ^{217}At)	^{213}Bi (incl. ^{213}Po)	^{209}Tl	^{209}Pb	^{227}Th	^{223}Ra (incl. ^{219}Rn, ^{215}Po)	^{211}Pb	^{211}Bi (incl. ^{211}Po)	^{207}Tl	^{211}At (incl. ^{211}Po)
K ← *K*	7.85E+00	1.80E+01	1.16E+01	5.51E-01	2.38E-01	8.05E+00	2.68E+01	4.24E-01	9.08E+00	4.47E-01	9.15E+00
C ← *C*	1.50E+01	3.42E+01	2.14E+01	5.94E-01	3.51E-01	1.53E+01	5.08E+01	4.80E-01	1.72E+01	4.92E-01	1.73E+01
OS ← *C*	3.35E-01	9.55E-01	1.08E+00	3.78E-01	1.00E-01	3.60E-01	1.42E+00	2.73E-01	5.39E-01	2.96E-01	5.02E-01
IS ← *C*	6.91E-04	2.41E-04	1.52E-01	2.72E-01	1.31E-02	2.42E-03	2.19E-03	1.64E-01	7.11E-03	1.88E-01	8.54E-04
IM ← *C*	6.40E-04	2.48E-04	1.26E-01	2.43E-01	9.87E-03	2.33E-03	2.16E-03	1.36E-01	5.84E-03	1.57E-01	7.83E-04
PP ← *C*	1.10E-01	3.15E-01	4.32E-01	2.63E-01	4.08E-02	1.19E-01	4.71E-01	1.66E-01	1.82E-01	1.86E-01	1.66E-01
K ← *C*	7.78E+00	1.78E+01	1.14E+01	4.70E-01	2.14E-01	7.97E+00	2.65E+01	3.60E-01	8.96E+00	3.78E-01	9.04E+00
C ← *OS*	3.35E-01	9.55E-01	1.08E+00	3.78E-01	1.00E-01	3.60E-01	1.42E+00	2.73E-01	5.39E-01	2.96E-01	5.02E-01
OS ← *OS*	2.41E+01	5.49E+01	3.44E+01	9.61E-01	5.68E-01	2.46E+01	8.16E+01	7.86E-01	2.75E+01	8.06E-01	2.78E+01
IS ← *OS*	7.25E-01	2.07E+00	2.27E+00	6.85E-01	1.89E-01	7.75E-01	3.08E+00	5.19E-01	1.14E+00	5.62E-01	1.09E+00
IM ← *OS*	4.77E-02	1.36E-01	5.20E-01	5.80E-01	1.03E-01	5.85E-02	2.13E-01	4.08E-01	1.44E-01	4.52E-01	7.26E-02
PP ← *OS*	6.46E-01	1.85E+00	1.94E+00	5.21E-01	1.33E-01	6.89E-01	2.75E+00	3.71E-01	9.93E-01	4.06E-01	9.72E-01
K ← *OS*	7.93E+00	1.83E+01	1.18E+01	6.11E-01	2.62E-01	8.13E+00	2.71E+01	4.74E-01	9.21E+00	5.00E-01	9.26E+00
C ← *IS*	6.91E-04	2.41E-04	1.52E-01	2.72E-01	1.31E-02	2.42E-03	2.19E-03	1.64E-01	7.11E-03	1.88E-01	8.54E-04
OS ← *IS*	7.25E-01	2.07E+00	2.27E+00	6.85E-01	1.89E-01	7.75E-01	3.08E+00	5.19E-01	1.14E+00	5.62E-01	1.09E+00
IS ← *IS*	5.49E+01	1.25E+02	7.88E+01	2.18E+00	1.39E+00	5.62E+01	1.86E+02	1.86E+00	6.29E+01	1.90E+00	6.35E+01
IM ← *IS*	1.11E+00	3.18E+00	3.65E+00	1.19E+00	3.70E-01	1.20E+00	4.75E+00	9.35E-01	1.82E+00	1.00E+00	1.67E+00
PP ← *IS*	4.56E-01	1.31E+00	1.52E+00	5.92E-01	9.27E-02	4.87E-01	1.95E+00	4.09E-01	6.98E-01	4.53E-01	6.92E-01
K ← *IS*	7.93E+00	1.83E+01	1.19E+01	6.91E-01	2.69E-01	8.13E+00	2.71E+01	5.31E-01	9.21E+00	5.64E-01	9.26E+00
C ← *IM*	6.40E-04	2.48E-04	1.26E-01	2.43E-01	9.87E-03	2.33E-03	2.16E-03	1.36E-01	5.84E-03	1.57E-01	7.83E-04
OS ← *IM*	4.77E-02	1.36E-01	5.20E-01	5.80E-01	1.03E-01	5.85E-02	2.13E-01	4.08E-01	1.44E-01	4.52E-01	7.26E-02
IS ← *IM*	1.11E+00	3.18E+00	3.65E+00	1.19E+00	3.70E-01	1.20E+00	4.75E+00	9.35E-01	1.82E+00	1.00E+00	1.67E+00
IM ← *IM*	4.40E+02	1.00E+03	6.19E+02	1.06E+01	8.84E+00	4.51E+02	1.49E+03	9.46E+00	5.02E+02	9.37E+00	5.07E+02
PP ← *IM*	1.60E+01	4.59E+01	4.24E+01	3.80E+00	2.12E+00	1.70E+01	6.82E+01	3.35E+00	2.38E+01	3.47E+00	2.41E+01
K ← *IM*	7.93E+00	1.83E+01	1.19E+01	7.06E-01	2.68E-01	8.13E+00	2.71E+01	5.35E-01	9.21E+00	5.69E-01	9.26E+00
C ← *PP*	1.10E-01	3.15E-01	4.32E-01	2.63E-01	4.08E-02	1.19E-01	4.71E-01	1.66E-01	1.82E-01	1.86E-01	1.66E-01
OS ← *PP*	6.46E-01	1.85E+00	1.94E+00	5.21E-01	1.33E-01	6.89E-01	2.75E+00	3.71E-01	9.93E-01	4.06E-01	9.72E-01
IS ← *PP*	4.56E-01	1.31E+00	1.52E+00	5.92E-01	9.27E-02	4.87E-01	1.95E+00	4.09E-01	6.98E-01	4.53E-01	6.92E-01
IM ← *PP*	1.60E+01	4.59E+01	4.24E+01	3.80E+00	2.12E+00	1.70E+01	6.82E+01	3.35E+00	2.38E+01	3.47E+00	2.41E+01
PP ← *PP*	5.71E+02	1.28E+03	7.74E+02	1.20E+01	1.01E+01	5.83E+02	1.91E+03	1.06E+01	6.42E+02	1.05E+01	6.48E+02
K ← *PP*	7.84E+00	1.80E+01	1.16E+01	6.02E-01	2.40E-01	8.04E+00	2.67E+01	4.53E-01	9.06E+00	4.81E-01	9.13E+00

TABLE S3. *S* values of some alpha emitters and their decay progenies.

$r_T \leftarrow r_S$	*S* values ($mGy.MBq^{-1}.s^{-1}$)											
	^{224}Ra	^{220}Rn (incl. ^{216}Po)	^{212}Pb	^{212}Bi (incl. ^{212}Po)	^{208}Tl	^{149}Tb	^{149}Gd	^{149}Eu	^{145}Eu	^{145}Sm	^{230}U	^{226}Th (incl. ^{222}Ra, ^{218}Rn, ^{214}Po)
K ← *K*	7.67E+00	1.76E+01	1.33E-01	1.10E+01	5.19E-01	9.92E-01	9.43E-02	3.55E-02	3.48E-02	4.50E-02	7.95E+00	3.73E+01
C ← *C*	1.46E+01	3.34E+01	2.28E-01	2.02E+01	5.66E-01	1.86E+00	1.57E-01	6.64E-02	4.79E-02	8.54E-02	1.52E+01	7.06E+01
OS ← *C*	3.18E-01	8.96E-01	2.92E-02	1.09E+00	3.51E-01	6.84E-02	2.46E-02	2.52E-03	1.60E-02	2.16E-03	3.46E-01	2.08E+00
IS ← *C*	7.51E-05	7.80E-06	1.48E-03	2.85E-01	2.33E-01	2.99E-02	4.49E-03	8.01E-04	1.25E-02	9.19E-04	3.35E-04	3.36E-04
IM ← *C*	7.82E-05	7.20E-06*	1.40E-03	2.62E-01	2.02E-01	2.67E-02	4.31E-03	7.45E-04	1.14E-02	8.64E-04	3.14E-04	3.32E-04
PP ← *C*	1.03E-01	2.95E-01	1.09E-02	5.16E-01	2.31E-01	3.79E-02	1.09E-02	1.31E-03	1.20E-02	1.24E-03	1.13E-01	6.89E-01
K ← *C*	7.60E+00	1.74E+01	1.26E-01	1.08E+01	4.41E-01	9.78E-01	8.90E-02	3.50E-02	3.17E-02	4.46E-02	7.87E+00	3.68E+01
C ← *OS*	3.18E-01	8.96E-01	2.92E-02	1.09E+00	3.51E-01	6.84E-02	2.46E-02	2.52E-03	1.60E-02	2.16E-03	3.46E-01	2.08E+00
OS ← *OS*	2.35E+01	5.37E+01	3.66E-01	3.24E+01	9.20E-01	2.98E+00	2.52E-01	1.07E-01	7.63E-02	1.37E-01	2.43E+01	1.13E+02
IS ← *OS*	6.87E-01	1.94E+00	5.53E-02	2.21E+00	6.50E-01	1.32E-01	4.52E-02	4.51E-03	2.76E-02	3.96E-03	7.48E-01	4.51E+00
IM ← *OS*	4.45E-02	1.25E-01	2.04E-02	6.77E-01	5.30E-01	6.86E-02	2.23E-02	2.65E-03	2.37E-02	2.11E-03	4.84E-02	2.95E-01
PP ← *OS*	6.12E-01	1.73E+00	4.42E-02	1.91E+00	4.79E-01	1.07E-01	3.49E-02	3.47E-03	2.19E-02	3.25E-03	6.67E-01	4.03E+00
K ← *OS*	7.74E+00	1.78E+01	1.40E-01	1.12E+01	5.79E-01	1.00E+00	9.99E-02	3.60E-02	3.70E-02	4.54E-02	8.03E+00	3.78E+01
C ← *IS*	7.51E-05	7.80E-06	1.48E-03	2.85E-01	2.33E-01	2.99E-02	4.49E-03	8.01E-04	1.25E-02	9.19E-04	3.35E-04	3.36E-04
OS ← *IS*	6.87E-01	1.94E+00	5.53E-02	2.21E+00	6.50E-01	1.32E-01	4.52E-02	4.51E-03	2.76E-02	3.96E-03	7.48E-01	4.51E+00
IS ← *IS*	5.36E+01	1.23E+02	8.60E-01	7.41E+01	2.14E+00	6.80E+00	5.91E-01	2.44E-01	1.70E-01	3.13E-01	5.55E+01	2.59E+02
IM ← *IS*	1.06E+00	2.99E+00	1.05E-01	3.53E+00	1.15E+00	2.19E-01	8.40E-02	8.28E-03	4.57E-02	6.63E-03	1.15E+00	6.94E+00
PP ← *IS*	4.31E-01	1.23E+00	2.86E-02	1.59E+00	5.35E-01	9.85E-02	2.52E-02	2.76E-03	2.48E-02	2.84E-03	4.70E-01	2.87E+00
K ← *IS*	7.74E+00	1.78E+01	1.41E-01	1.13E+01	6.52E-01	1.01E+00	1.01E-01	3.62E-02	4.01E-02	4.56E-02	8.03E+00	3.78E+01
C ← *IM*	7.82E-05	7.20E-06*	1.40E-03	2.62E-01	2.02E-01	2.67E-02	4.31E-03	7.45E-04	1.14E-02	8.64E-04	3.14E-04	3.32E-04
OS ← *IM*	4.45E-02	1.25E-01	2.04E-02	6.77E-01	5.30E-01	6.86E-02	2.23E-02	2.65E-03	2.37E-02	2.11E-03	4.84E-02	2.95E-01
IS ← *IM*	1.06E+00	2.99E+00	1.05E-01	3.53E+00	1.15E+00	2.19E-01	8.40E-02	8.28E-03	4.57E-02	6.63E-03	1.15E+00	6.94E+00
IM ← *IM*	4.31E+02	9.80E+02	6.28E+00	5.82E+02	1.04E+01	5.41E+01	4.25E+00	1.94E+00	1.11E+00	2.51E+00	4.45E+02	2.07E+03
PP ← *IM*	1.52E+01	4.31E+01	8.84E-01	3.80E+01	3.88E+00	1.63E+00	5.87E-01	4.95E-02	1.49E-01	4.82E-02	1.66E+01	1.00E+02
K ← *IM*	7.74E+00	1.78E+01	1.41E-01	1.13E+01	6.61E-01	1.01E+00	1.01E-01	3.62E-02	4.08E-02	4.57E-02	8.03E+00	3.78E+01
C ← *PP*	1.03E-01	2.95E-01	1.09E-02	5.16E-01	2.31E-01	3.79E-02	1.09E-02	1.31E-03	1.20E-02	1.24E-03	1.13E-01	6.89E-01
OS ← *PP*	6.12E-01	1.73E+00	4.42E-02	1.91E+00	4.79E-01	1.07E-01	3.49E-02	3.47E-03	2.19E-02	3.25E-03	6.67E-01	4.03E+00
IS ← *PP*	4.31E-01	1.23E+00	2.86E-02	1.59E+00	5.35E-01	9.85E-02	2.52E-02	2.76E-03	2.48E-02	2.84E-03	4.70E-01	2.87E+00
IM ← *PP*	1.52E+01	4.31E+01	8.84E-01	3.80E+01	3.88E+00	1.63E+00	5.87E-01	4.95E-02	1.49E-01	4.82E-02	1.66E+01	1.00E+02
PP ← *PP*	5.59E+02	1.26E+03	7.42E+00	7.31E+02	1.17E+01	7.11E+01	5.11E+00	2.57E+00	1.40E+00	3.33E+00	5.77E+02	2.64E+03
K ← *PP*	7.65E+00	1.76E+01	1.33E-01	1.10E+01	5.61E-01	9.96E-01	9.50E-02	3.56E-02	3.69E-02	4.51E-02	7.93E+00	3.72E+01

* Simulation error within 10%.

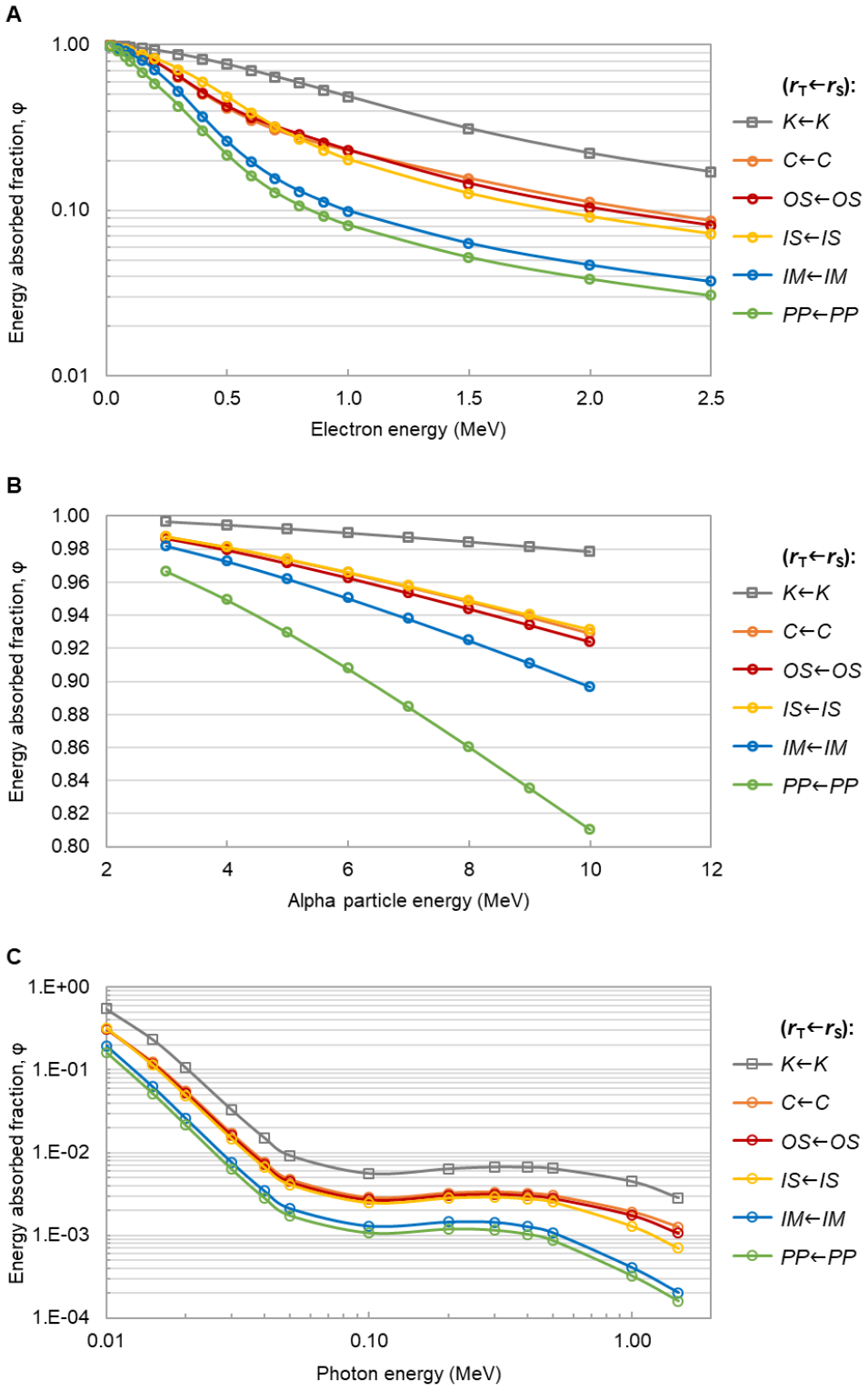

FIGURE S2. Energy absorbed fractions (φ) for monoenergetic electrons (**A**), monoenergetic alpha particles (**B**) and monoenergetic photons (**C**), for self-irradiation. Data points are connected by smooth lines.

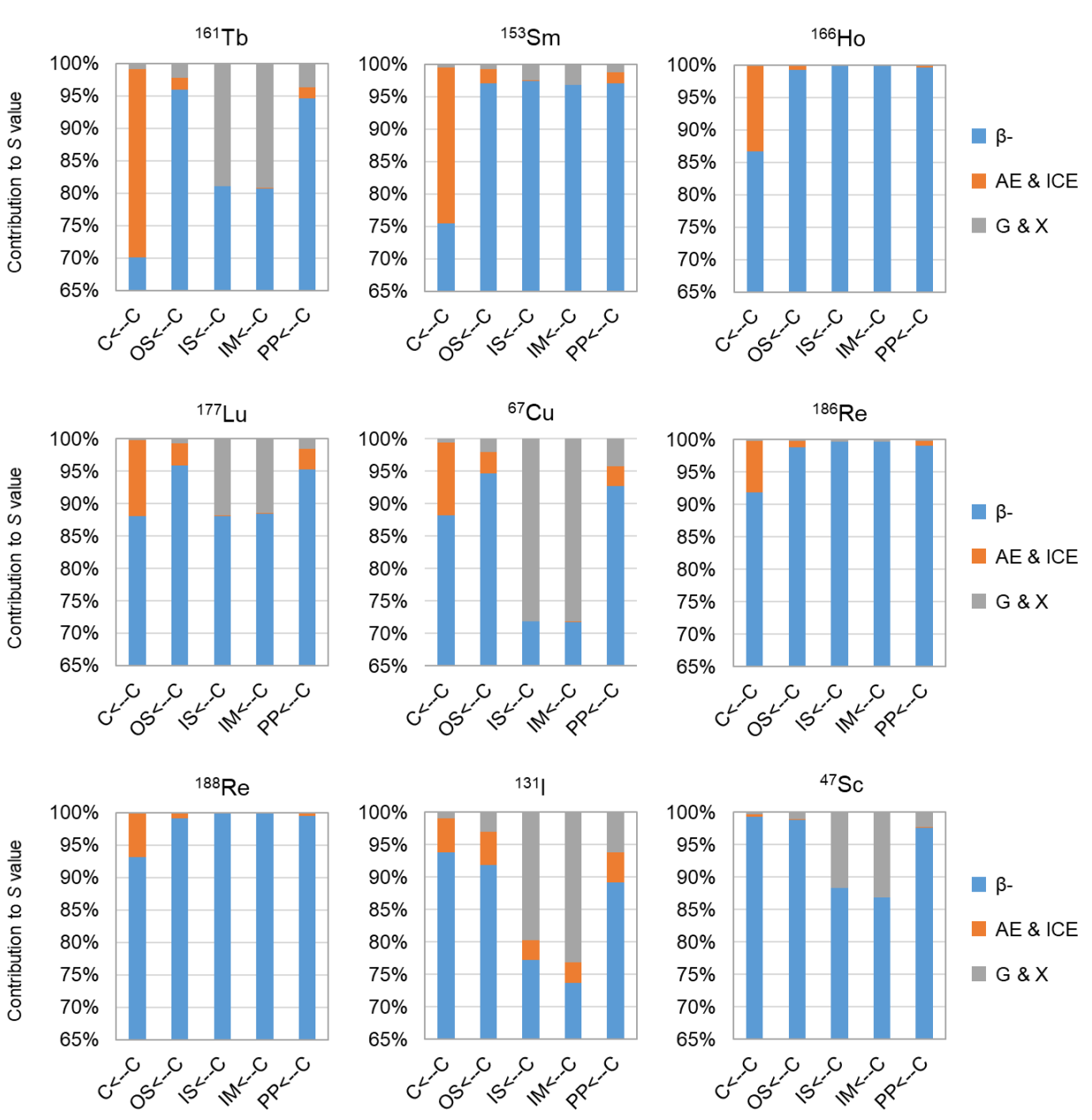

FIGURE S3. Contribution of different radiation types (AE & IEC: Auger and internal conversion electrons; β-: beta- particles; G & X: gamma- and X-rays) to the *S* values of some beta emitters.

TABLE S4. Fraction of injected activity per gram (*FIA/g*) of dissected kidney and percentage of the normalized whole kidney activity (A_{kidney_norm}) allocated to each source tissue region, for the different time points of the ^{131}I-sdAb pharmacokinetics.

Time point (*h*)	*FIA/g* (g^{-1})	$A(r_S)/A_{kidney\_norm}$ *100 (*%*)				
		C	*OS*	*IS*	*IM*	*PP*
1	4.36E-01	43%	50%	6%	<1%	<1%
3	5.32E-02	32%	60%	8%	<1%	<1%
6	1.82E-02	37%	56%	6%	1%	<1%
24	1.48E-03	69%	26%	4%	<1%	<1%
70	4.92E-04	63%	26%	10%	<1%	<1%

TABLE S5. Coefficients of the power functions used to fit the time–absorbed dose rate per injected activity data of each target tissue region, for the two source distributions considered. R^2 values were always > 0.999.

r_S	r_T	Function coefficients	
		c_1 ($mGy.h^{-1}.MBq^{-1}$)	c_2
K (unif)	*K*	43.8	1.89
non-unif	*K*	44.4	1.87
non-unif	*C*	36.9	2.02
non-unif	*OS*	62.8	1.78
non-unif	*IS*	34.2	1.76
non-unif	*IM*	26.7	1.90
non-unif	*PP*	26.1	1.85

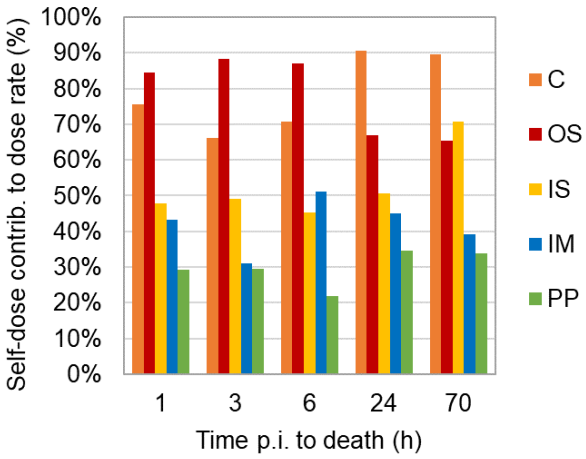

FIGURE S4. Contribution of self-irradiation to the time-dependent absorbed dose rate of different kidney tissue regions (*C*, *OS*, *IS*, *IM*, *PP*).